RSC Advances

PAPER

View Article Online
View Journal | View Issue

Cite this: *RSC Adv.*, 2020, **10**, 19542

Synthesis and characterization of TiO_2/$Mg(OH)_2$ composites for catalytic degradation of CWA surrogates†

Martin Šťastný, *[ab] Václav Štengl,[a] Jiří Henych,[a] Jakub Tolasz,[ab] Martin Kormunda,[c] Jakub Ederer,[b] Gloria Issa[d] and Pavel Janoš[b]

Received 3rd February 2020
Accepted 6th May 2020

DOI: 10.1039/d0ra00944j

rsc.li/rsc-advances

Surface catalyzed reactions can be a convenient way to deactivate toxic chemical warfare agents (CWAs) and remove them from the contaminated environment. In this study, pure titanium oxide, magnesium hydroxide, and their composites TiO_2/$Mg(OH_2)$ were prepared by thermal decomposition and precipitation of the titanium peroxo-complex and/or magnesium nitrate in an aqueous solution. The as-prepared composites were examined by XRD, XPS, HRTEM, and nitrogen physisorption. Their decontamination ability was tested on CWA surrogates and determined by high-performance liquid chromatography (HPLC) and gas chromatography coupled with mass spectrometry (GC-MS). Dimethyl methyl phosphonate (DMMP) was used as a G simulant for the nerve agents sarin (GB) and soman (GD) while 2-chloroethyl ethyl sulfide (2-CEES) and 2-chloroethyl phenyl sulfide (2-CEPS) were used as surrogates of sulfur mustard (HD). The activity of the as-prepared composites was correlated with acid–base properties determined by potentiometric titrations and pyridine adsorption studied by *in situ* DRIFTS. The mixing of Ti and Mg led to an increase of the surface area and the amount of surface –OH groups (with an increasing amount of Ti) that caused improved degradation of DMMP.

Introduction

Chemical warfare agents (CWAs) are a group of hazardous chemicals whose deleterious effects have been deliberately used against humans to damage the essential physiological functions of the body.[1] CWAs include blistering agents (yperites), asphyxiating agents (phosgene), and nerve agents (acetylcholinesterase enzyme inhibitors).[2]

For detoxification and decontamination of the environment affected by CWAs, various chemical agents (NaOH, NaClO, $Ca(ClO)_2$) utilizing mostly hydrolytic and oxidation reactions are used. Advantageously, these reactions may be employed under relatively mild conditions (ambient temperature, atmospheric pressure), and the degradation products formed can be either burned or bituminized.[3] However, their use may be limited due to the generation of significant amounts of liquid waste. In recent years, the unique nanostructured materials (called "reactive sorbents" or "destructive adsorbents") have been developed. They can efficiently bind and destroy certain dangerous chemicals, including toxic organophosphate nerve agents sarin,[4–6] soman,[7–9] VX,[10–12] or organophosphorus pesticides,[13–15] and rapidly decompose them into non-toxic or less toxic products. The surface catalysis of CWAs, their surrogates, or related environmental pollutants, such as pesticides, was documented on pure nanostructured metal oxides MgO,[16,17] CaO,[10] TiO_2,[9] Mn_xO_y,[18] Fe_2O_3,[19] Al_2O_3 (ref. 20) or CeO_2.[15]

Their excellent activity stems from a combination of their high specific surface area (~hundreds m2 g^{-1}), suitable porosity, and a large number of shape dislocations (edges, corners) and structural defects that can act as active sites for adsorption and chemical degradation.[21] Nanoscale magnesium oxide (MgO) is a well-known basic oxide that readily reacts with organophosphorus compounds at ambient temperatures by stoichiometric degradation.[22,23] The so-called nanocrystalline Mg oxides (AP-MgO) can be prepared by high-temperature supercritical drying firstly described by Klabunde *et al.* (2001).[24] This method is based on hydrolysis of organometallic compounds, mostly alcoholates (*e.g.*, magnesium methoxide $Mg(OCH_3)_2$), followed by supercritical drying in an autoclave in a mixture with toluene at 265 °C. These materials were efficient

[a]*Institute of Inorganic Chemistry of the Czech Academy of Sciences, 250 68, Řež, Czech Republic*

[b]*Faculty of Environment, University of Jan Evangelista Purkyně in Ústí nad Labem, Králova výšina 3132/7, 400 96 Ústí nad Labem, Czech Republic*

[c]*Faculty of Science, University of Jan Evangelista Purkyně in Ústí nad Labem, České mládeže 8, 400 96 Ústí nad Labem, Czech Republic*

[d]*Institute of Organic Chemistry with Centre of Phytochemistry, Bulgarian Academy of Sciences, Ak. G. Bontchev str., bl.9, Sofia, 1113, Bulgaria*

† Electronic supplementary information (ESI) available: Detailed material characterization along with supplementary figures, XRD patterns, adsorption isotherms, XPS spectra, TEM and HRTEM micrographs, GC chromatograms and the appropriate *m*/*z* spectra of CWA surrogates, and kinetic curves and kinetic parameters for the degradation of other CWA surrogates in an aqueous solution. See DOI: 10.1039/d0ra00944j

for destructive adsorption of 2-CEES. Similarly, MgO nanoparticles with a surface area up to 1236 $m^2 g^{-1}$ were prepared by Štengl *et al.* (2003).[25]

Furthermore, the specific activity of these sorbents can be improved by formation of mixed or doped oxides and nanocomposites. Thus-prepared materials may have better catalytic properties due to their morphology and structural features, large specific surface, or more active sites.[26,27] Metallocene Ziegler-Natta Ti/Mg-mixed catalysts are studied for producing commercially essential polymers such as polypropylene (PP) by radical or ionic polymerization.[28] The detailed study of structural properties of Ti/Mg mixed oxides or composites prepared by various methods were reported in several recent studies. Liu *et al.* (2014) described the synthesis of Mg/Ti nanocomposites by co-precipitation of anhydrous magnesium chloride ($MgCl_2$), titanium tetrachloride ($TiCl_4$) and lithium naphthalide (LiNp) in tetrahydrofuran (THF) solution for rapid hydrogen absorption at room temperature.[29] Depending on synthesis procedure, various Ti and Mg oxide phases can be obtained, such as hexagonal MgO and tetragonal γ-TiH_2 phases forming irregularly shaped particles aggregating together,[29] crystalline MgO and anatase TiO_2 with mesoporous structures containing spherical nanoparticles[30] or nanocomposite rods representing MgO, TiO_2, $MgTiO_3$, and Mg_2TiO_4 crystal forms.[31] These materials are mostly used for adsorption of heavy metals,[32,33] photocatalytic degradation of organic azo dyes,[34,35] or in dye-sensitized solar cells.[36,37] Nevertheless, their use in catalytic degradation of CWA surrogates was not reported yet.

In this work, TiO_2/$Mg(OH)_2$ nanocomposites were prepared by simple thermal hydrolysis of titanium peroxo-complexes in an aqueous solution. The as-prepared catalysts were tested for degradation of CWA surrogates (DMMP, 2-CEES, and 2-CEPS) in water evaluated by chromatographic methods (HPLC, GC-MS) and *in situ* DRIFTS spectroscopy.

Materials

Titanium oxo-sulfate ($TiOSO_4$), magnesium nitrate ($Mg(NO_3)_2$), sodium hydroxide (NaOH), ammonia solution (NH_4OH), and hydrogen peroxide, 30% (H_2O_2) were purchased from Sigma-Aldrich (Czech Republic). Pyridine (99,5%, p.a.) was obtained from Verkon, Czech Republic. Nerve agent surrogates dimethyl methylphosphonate (DMMP), 2-chloroethyl ethyl sulfide (2-CEES), and 2-chloroethyl phenyl sulfide (2-CEPS) were purchased from Sigma-Aldrich as chromatographic standard (>97%). HPLC organic solvents (Fischer scientific, Czech Republic) were used to prepare the solutions, including the mobile phases for liquid chromatography.

Experimental

TiO_2/$Mg(OH)_2$ based catalysts were prepared according to the scheme shown in Fig. S1.† Further details are given in Sections S1–S3 of the ESI.†

Powder X-ray diffraction (PXRD) patterns were obtained using Bruker D2 diffractometer equipped with a conventional X-ray tube (Cu Kα radiation, 30 kV, 10 mA) and the LYNXEYE 1-dimensional detector. The primary divergence slit module width 0.6 mm, Soler Module 2.5, Airscatter screen module 2 mm, Ni Kbeta-filter 0.5 mm, step 0.00405°, and time per step 0.3 s were used. The qualitative analysis was performed with a DiffracPlus Eva software package (Bruker AXS, Germany) using a JCPDS PDF-2 database. The crystallite sizes were calculated from diffraction line broadening using the Scherrer formula:[38]

$$a = \frac{K\lambda}{\beta \cos \theta} \quad (1)$$

where K is the shape factor, λ is the wavelength of the applied radiation, β is the broadening of the diffraction line, and θ is the diffraction angle.

The specific surface area and porosity of the powder samples were measured using a Quantachrome NOVA 4200e instrument at liquid nitrogen temperature. The samples were degassed for 6 hours at 150 °C. The Brunauer–Emmett–Teller (BET) method was used for surface area calculation. The BJH method (Barrett, Joyner, and Halenda) was used for calculating pore size distributions.[39]

X-ray photoelectron spectroscopy (XPS) measurements were performed using a SPECS PHIBOS 100 hemispherical analyzer with a 5-channel detector and a SPECS XR50 X-ray source equipped with an Al anode. The calibration of the binding energy (BE) was performed using the C 1s main component set to 285 eV. Survey spectra were recorded with a pass energy of 40 eV, and the high-resolution spectra were recorded as a sum of 10 acquisitions with a pass energy of 10 eV. A Shirley background profile was used for data processing in CasaXPS software. The charge compensation was made by a C 1s peak calibration process. The C 1s peaks have a single peak character attributed to C–C bonds and calibrated to the binding energy (BE) of 284.8 eV.

The morphology of the samples was inspected by transmission electron microscopy (TEM) using a 200 kV TEM microscope FEI Talos F200X. A microscopic 300-Mesh Regular Copper Grid coated with a thin transparent silicon dioxide (SiO_2)/monoxide (SiO) was used for the preparation of samples.

Adsorption/degradation tests were performed using a nerve-agent surrogate as an internal standard (0.095 mg mL^{-1} in deionized water). In this procedure, 0.03 g of the catalyst was mixed with 0.5 mL water and 0.5 mL of the nerve-agent surrogate standard in a series of covered vials (Eppendorf, 2 mL) by aluminum foil protected to sun-light. At pre-determined time intervals (0, 5, 15, 20, 30, 50, 70, 90, and 120 min), the reaction was terminated by the addition of 0.5 mL of formic acid (0.1%), and the powder catalyst was separated by centrifugation (10 000 rpm, 2.5 min).

Photocatalytic tests were carried out in a batch arrangement in a laboratory air-cooled UV-box without external light access. Three UV lamps (PL-S 230 V/11 W, HADEX, s.r.o., Czech Republic) with the maximum radiation at 365 nm were used. All photodegradation experiments were performed in aqueous solutions (10 mL) at the same initial CWA surrogate concentration (0.095 mg mL^{-1}) and catalyst dose (150 mg). Photocatalytic experiments were carried out at room temperature and

without pH adjustment. A round bottom crystallization dish was used as the reaction vessel.

The supernatant was analyzed immediately by high-performance liquid chromatography (HPLC). All catalytic experiments were conducted at the laboratory temperature of 22 ± 1 °C. In each series of measurements, several types of quality control experiments were performed: Blank experiments without the presence of powder catalysts.

The surface acidity of the catalysts was investigated by adsorption of pyridine (Py) vapours at room temperature (30 °C). Powder sample was placed in DRIFT cell, heated at 150 °C for 30 min, and cooled to room temperature (30 °C) under constant flow (100 mL min^{-1}) of nitrogen gas. Then the Pyridine was dosed for 5 min using flow of nitrogen through saturator with liquid Py, and then the DRIFT cell was flushed with pure Nitrogen for 15 min. FTIR spectra were recorded using a Thermo Nicolet NEXUS 670 FTIR spectrometer, equipped with a nitrogen-cooled detector and accumulating 64 scans at a spectral resolution of 4 cm^{-1}.

The concentration of CWAs surrogates was determined by liquid chromatography using a Dionex UltiMate® 3000 U-HPLC system with Diode Array Detector (DAD) operating at 230 nm, Rheodyne 7725i injection valve with a 20 μL sampling loop, and a Hypersil GOLD column (Thermo ScientificTM) 250 × 4.6 mm, packed with a C18 stationary phase, 5 μm. Acetonitrile (HPLC-gradient grade, Thermo Fischer Scientific) with the addition of formic acid (0.1%)/water acidified with formic acid (0.1%) was used as mobile phase with a set gradient from −1.5 minute up to 0 minutes for the column equilibration and from 0 minutes (30% acetonitrile) up to 10 minutes (95% acetonitrile), at a flow rate of 1.2 mL min^{-1} and the column temperature of 30 °C.

A portion of the resulting supernatants obtained after the catalytic reaction was adjusted by a static headspace after the establishment of the equilibrium state between the liquid and vapor phase. The gas-phase was collected using a Hamilton gas-tight syringe and immediately injected into the gas chromatograph with mass spectrometry (GC-MS). The gas chromatograph was an Agilent 6890N model with an HP-5 column 19091J-413 (5%-phenyl-methylpolysiloxane, 30 m × 0.32 mm I.D. × 0.25 μm film thickness), and mass spectrometry (MS) JEOL JMS-Q100GC was used for the identification of the main degradation products of the surrogates. The operation was carried out in an electronic impact (EI) ionization mode. Helium (99.999%) was the carrier gas at the flow rate of 2.0 mL min^{-1}. The temperature program for the chromatographic run (after optimization) was the following: $T_0 = 40$ °C; $T_0 - T_1$, 20°C min^{-1}, $T_1 = 260$ °C (hold time, 6 min). The injection was set to a splitless mode at 200 °C; the injection volume was 1.0 μL; the total run time was ∼20.00 min. The EI ionization was performed at an electron energy of 70 eV, and *m*/*z* ratio 50–200 was recorded in the full-scan mode.

DMMP adsorption on the surface of the catalyst (Ti050Mg050) at ambient temperature was observed by FTIR diffuse reflectance spectroscopy (DRIFTS) using a Thermo Nicolet NEXUS 670 FTIR spectrometer. In a typical experiment,[40,41] the powder sample was placed in a DR cuvette (Praying Mantis, Harrick) and a droplet (5 μL) of a liquid DMMP (97%, Sigma Aldrich) was dosed by an automatic micropipette. The acquisition of spectra was started immediately and repeated in selected time intervals (0, 15, 30, 50, 90, and 120 min). All presented spectra were processed using OMNIC Spectra software.

Acid–base potentiometric titrations were performed on an automatic titrator controlled by a PC (794 Basic Titrino, Metrohm, Switzerland) with a potentiometric endpoint determination. Typically, 75 mg of sample catalyst was weighed into the titration vessel, 30 mL of NaCl was added (0.1 mol L^{-1}), 3 mL of a standardized solution of HCl (0.1 mol L^{-1} in 0.1 mol L^{-1} NaCl) and the suspension was mixed and bubbled by nitrogen for 30 minutes. Subsequently, the samples were titrated with standardized 0.1 mol L^{-1} NaOH (in 0.1 mol L^{-1} NaCl) with continuous stirring with a magnetic bar under nitrogen atmosphere. The rate of titrant was 0.1 mL min^{-1} in 0.05 mL aliquots.

Results and discussion

Materials characterization

By combining titanium oxide and magnesium hydroxide, a nanocomposite material with a very well-defined structure, a high specific surface area, and a high proportion of reactive sites has been obtained. By mixing the appropriate amount of TiO_2 and $Mg(OH)_2$, the acid–base properties, as well as the specific surface area of the resulting material can be effectively controlled. The $TiO_2/Mg(OH)_2$ composites were prepared by thermal decomposition and precipitation of titanium peroxo-complex and/or magnesium nitrate in an aqueous solution as described in detail in ESI S1, S2, and S3.†

Compared to pure oxides or hydroxides, respectively, the activity of the resulting materials for CWA surrogates degradation can be increased several times, as shown below. Herein, the as-prepared $TiO_2/Mg(OH)_2$ composites were denoted as TiXXXMgYYY, where XXX and YYY represent the percentage ratio of TiO_2 and $Mg(OH)_2$, respectively (see Table S1†). The as-prepared composites were examined by XRD, XPS, HRTEM, and nitrogen physisorption.

The results of the material characterization are given in ESI S4† (X-ray powder diffraction, XRD) and S5 (nitrogen physisorption), respectively.

The XPS data provided information about the surface chemical states of Ti, Mg, and O in mixed $TiO_2/Mg(OH)_2$ composites (Table S4 and ESI Fig. S4–S6†). In the Mg 2p region of the samples Ti020Mg080 and Ti000Mg100 (see Fig. S4†), the peak found at binding energy ∼49 eV indicates presence of $Mg(OH)_2$ phase.[42,43] Higher Ti concentration in the samples (Ti050Mg050, Ti080Mg020) leads to the broadening and shifting of the peak to lower energies indicating strong interaction of Ti and Mg ions. Ti 2p peaks (see Fig. S6†) with the binding energies at 464–458 eV (samples marked as Ti100Mg000, Ti080Mg020, and Ti050Mg050) were assigned to TiO_2. However, the Ti2p doublet in Ti080Mg020 but mainly in Ti050Mg050 was significantly shifted to a lower BE, which suggests, again, strong interaction of Ti^{3+} with Mg^{2+}. The Ti2p peaks were also tentatively deconvoluted to single TiO_2 phase peaks with minor

contributions of sub-stoichiometric $Ti^{x<4+}$ oxides with BE *ca.* 456.2 and 457.7 eV.[44] In the sample with 20% Ti, the Ti 2p peaks were completely missing suggesting that the Ti phase is covered by $Mg(OH)_2$ overlayer. The O 1s deconvoluted peak (Fig. S6†) of pure titania with maximum at 530 eV correspond to Ti–O bond (a lattice oxygen peak O^{2-}) while binding energy of 532 eV corresponds to surface Ti–OH bond. In the O 1s spectra of the samples with higher magnesium content, dominates the peak with a maximum at ~531 eV that may be associated principally with the presence of oxygen in magnesium hydroxide.[45] Nevertheless, the detailed deconvolution and assignment of the peaks is challenging due to the complexity of the oxygen species present in the samples.

TEM and HRTEM micrographs of the $TiO_2/Mg(OH)_2$ samples (see ESI Fig. S7–S9†) showed spindle-like nanoparticles, typical for thermal hydrolysis of Ti peroxo-complexes as has been previously reported,[46] with $Mg(OH)_2$ plate-like overlayer. This is already evident in the sample with the lowest titanium content (Ti020Mg080). High-resolution analysis (in Fig. 1) of the sample Ti050Mg050 revealed the interplanar distances 0.344 and 0.823 nm which correspond to the planes (0 1 1) of anatase and to (0 0 1) of brucite, as inferred from the diameter of the diffraction rings obtained from the Fast Fourier Transform (FFT). The calculated interplanar distances for other samples are 0.242 nm for the Ti020Mg080 sample, which corresponds to (0 0 2) plane of brucite. For Ti080Mg020, 0.205 and 0.211 nm distances correspond to (0 1 2) plane of brucite while distances 0.238 and 0.378 nm were assigned to (0 0 4) and (0 1 1) planes of anatase, respectively. 0.190 and 0.355 nm distances found in the Ti100Mg000 sample belong to (0 2 0) and (0 1 1) planes of anatase. The elemental composition obtained from the TEM/EDS mapping is presented in Table S2.†

Degradation tests. The composites were tested for the degradation of CWA surrogates in an aqueous solution by procedure used in our previous studies.[47] The obtained experimental data were fitted using the pseudo-first-order kinetic eqn (2):

$$q_t = q_1 \exp(-kt) + q_\infty \quad (2)$$

where q_t is the residual amount of surrogate in time t, k is the pseudo-first-order rate constant, q_1 is the fraction of surrogate degraded during the degradation experiment, and q_∞ is the residual (unconverted) amount of surrogate in infinite time. The kinetic parameters were estimated using a non-linear analysis (see Table 1).

The normalized kinetic curves for DMMP degradation in the dark on TiO_2 and $Mg(OH)_2$ and their composites are presented in Fig. 2. Interestingly, the degradation efficiency of the composites is higher than those of pure TiO_2 and $Mg(OH)_2$. As can be seen in Table 1, the rate constant k for DMMP degradation on the most active sample (Ti080Mg020) is ~0.078 min^{-1}, which corresponds to reaction half-time ($\tau_{1/2}$) *ca.* 9 min. The relatively high activity was also observed for other composites ranging from 0.061 (Ti020Mg080) to 0.065 min^{-1} (Ti050Mg050) with reaction half-times ($\tau_{1/2}$) ~11 minutes. Fig. S12A and B† show the dependency of the rate constant and degree of DMMP conversion after 120 min, respectively, on the surface area of the samples. As can be concluded, the mixing of Ti and Mg leads to an increase of the specific surface area (SA) that results in improvement of both degradation rate and efficiency. The most active sample for DMMP degradation (Ti080Mg020, $k_{DMMP} \sim 0.78$ min^{-1}) had also the highest specific surface area (~223 m^2 g^{-1}) and porosity (~0.40 cm^3 g^{-1}). On the other hand, the Ti050Mg050 sample had the highest degree of DMMP conversion (~98%) after 120 min, which indicate that also the qualitative surface properties are important as will be discussed further below.

Sample Ti050Mg050 was further tested for degradation of sulphur mustard (yperite) surrogates 2-CEES and 2-CEPS (see Table S5†). The rate constant for 2-CEES degradation was 0.115 min^{-1} and degree of conversion ~79.5% after 120 minutes. The degradation of 2-CEPS was more efficient and reached nearly 95% conversion within 120 minutes but the rate constant was more than two times smaller 0.047 min^{-1} with half-life ~15 min. Kinetic curves for 2-CEES and 2-CEPS degradation are shown in Fig. S10.†

Influence of acid–base properties. The acidity/basicity of metal oxide catalysts is the ability of a metal oxide to transform an adsorbed base into its conjugated acid or *vice versa*. The reaction is based on proton transfer from the surface of the material to the adsorbate (Brønsted acidity), or the electron pair from the adsorbate to the surface of the material (Lewis acidity).[48]

In an aqueous environment, metal oxides are covered with surface hydroxyl groups (S–OH^0), whereas the presence of two lone electron pairs and dissociable hydrogen ion indicates that these groups are ampholytic. Adsorption of H^+ and OH^- ions is thus based on protonation and deprotonation of surface hydroxyls, as shown by eqn (3) and (4), where S represents the surface of the material:[49,50]

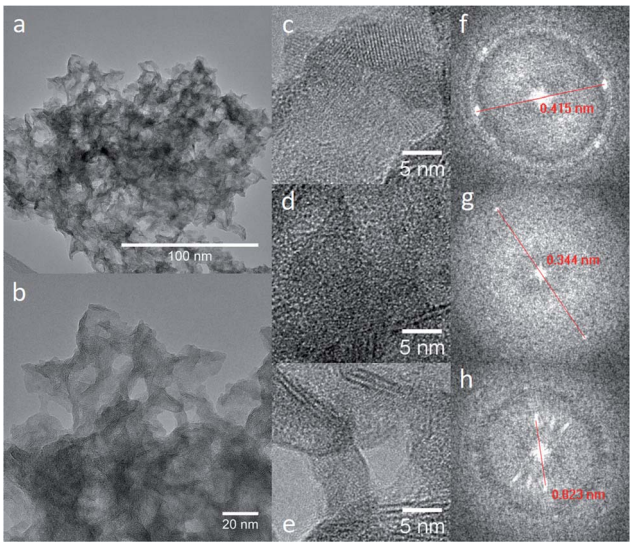

Fig. 1 TEM (a) and HRTEM (b–e) micrographs of sample marked as Ti050Mg050. Insets (f–h) give a magnification of selected areas and appropriate FFR patterns.

Table 1 Kinetic parameters for the catalytic degradation of DMMP in water on the surface of the prepared samples

	Catalytic degradation of DMMP in water			Qualitative parameters	
Sample	$k \pm$ SE[a] (min^{-1})	$\tau_{1/2}$[b] (min)	d[c] (% 120 min^{-1})	[d]R^2	SEE[e]
Ti000Mg100	0.022 ± 0.008	31.5	52.2	0.9819	0.007
Ti020Mg080	0.061 ± 0.006	11.3	90.3	0.9902	0.001
Ti050Mg050	0.065 ± 0.004	10.7	98.4	0.9937	0.008
Ti080Mg0200	0.078 ± 0.009	8.9	91.2	0.9839	0.002
Ti100Mg000	0.016 ± 0.007	43.3	41.8	0.9700	0.007

[a] SE is the standard error of the estimated parameter. [b] $\tau_{1/2}$ is the half-life time of the decaying quantity DMMP (min). [c] d is the degree of DMMP conversion after 120 minutes (%). [d] R^2 is the determination coefficient obtained by fit. [e] SEE is the standard error of the estimate.

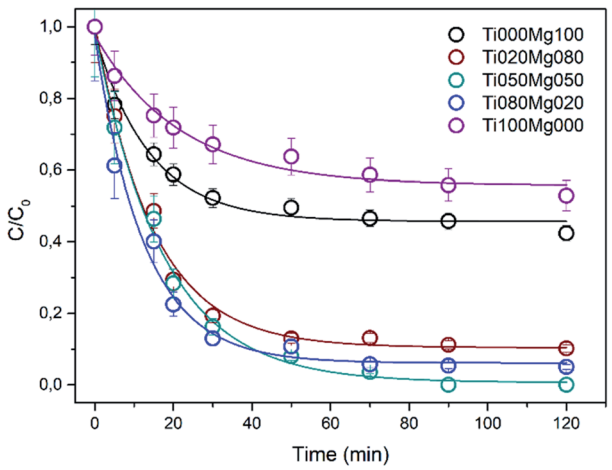

Fig. 2 Kinetic curves of DMMP degradation on TiO_2, $Mg(OH)_2$, and their composites.

$$\equiv S\text{–}OH^0 + H^+ \leftrightarrow S\text{–}OH_2^+ \quad (3)$$

$$\equiv S\text{–}OH^0 \leftrightarrow S\text{–}O^- + H^+ \quad (4)$$

The pH at which the concentrations are equal $[S\text{–}O^-] = [S\text{–}OH_2^+]$ is known as point zero charge (pH_{PZC}).[51]

The acidity/basicity and the point of zero charge (PZC) of TiO_2/$Mg(OH)_2$-based composites were determined by direct titration with a potentiometric endpoint determination.

The point of zero charge (PZC) has been evaluated from titration curves which have been transformed into curves corresponded to the total concentration of protons consumed in the titration process (TOTH) and can be calculated from the following equation:[52]

$$\mathrm{TOTH} = \frac{-(V_{\mathrm{NaOH}} - V_{\mathrm{EP1}})c_{\mathrm{NaOH}}}{m} \quad (5)$$

where c_{NaOH} represents the concentration of NaOH [mol L^{-1}], V_{EP1} represents the volume of first equivalent point [L], V_{NaOH} [L] represents the consumption of NaOH at individual titration points, m is the amount of catalyst used in the titration [g].

The amount of surface hydroxyl groups per solid weight of catalyst (q-OH) was calculated from the two equivalence points of the titration curve (V_{EP1} and V_{EP2}) by the following formula:

$$q_{-\mathrm{OH}} = \frac{(V_{\mathrm{EP2}} - V_{\mathrm{EP1}})c_{\mathrm{NaOH}}}{m} \quad (6)$$

The amount of consumed OH^- to reach pH value 10.5, the amount of surface hydroxyl groups (q-OH), and pH_{PZC} are summarized in Table 2.

The titration curves of TOTH *vs.* pH calculated according to eqn (5) for TiO_2/$Mg(OH)_2$ composites are shown in Fig. 3.

As can be seen in Fig. 3 and Table 2, the amount of hydroxyl ions (OH^-) consumed during the titration process (to reach pH value 10.5) increase in the order Ti000Mg100 < Ti100Mg000 < Ti020Mg080 < Ti080Mg020 < Ti050Mg050. In general, the amount of hydroxyl groups (OH–) consumed during titration are directly related to the buffering capacity of the catalysts. The sample denoted as Ti000Mg100 (pure magnesium hydroxide) showed the lowest capacity while sample denoted as Ti050Mg050 has the highest capacity.

TOTH curves were used for the estimation of samples pH corresponding to the PZC values. The higher content of magnesium hydroxide (Ti020Mg080 and Ti000Mg100) significantly increases the initial pH of the solution. In general, at pH < pH_{PZC}, the surfaces of composites were positively charged, while at pH > pH_{PZC}, the surfaces of composites were negatively charged.

Fig. 3 shows that at pH < 5, the surfaces of composites with higher Ti content (Ti100Mg000, Ti080Mg020 and Ti050Mg050) were positively charged, and at pH > 5, they were negatively charged. However, composites with higher Mg content (Ti020Mg080 and Ti000Mg100) were positively charged at pH <

Table 2 The amount of consumed OH– during titration (to reach pH = 10.5) process and $pH_{(PZC)}$ calculated from the TOTH curve and amount of hydroxyl groups (q-OH)

Sample	Consumed OH– [mmol g^{-1}]	q-OH [mmol g^{-1}]	$pH_{(PZC)}$
Ti100Mg000	1.05	0.265	5.01
Ti080Mg020	2.89	0.717	4.77
Ti050Mg050	4.35	0.497	4.78
Ti020Mg080	1.67	0.151	9.34
Ti000Mg100	0.91	0.152	9.85

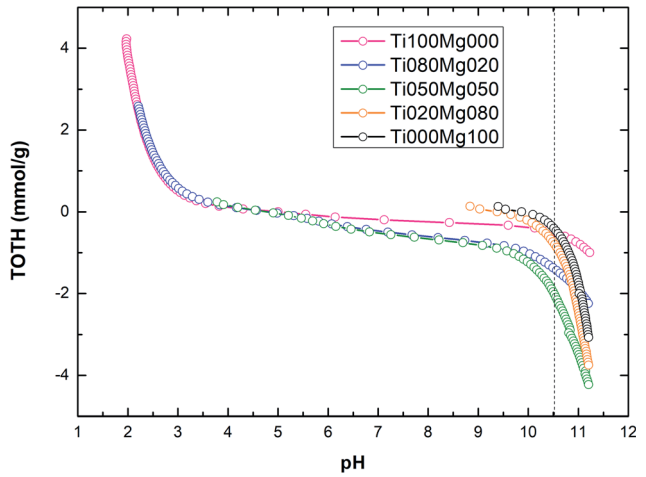

Fig. 3 TOTH curves of the prepared samples as a function of pH.

10, and at pH > 10 were negatively charged. As can be seen from Table 2, the higher Mg(OH)2 content, as well as higher basicity of samples (pH_{PZC} ~9.3–9.9), can be ascribed to higher amount of unsaturated oxygen atoms coordinated to the Mg atoms.[53] The calculated pH_{PZC} values are in accordance with some of the previous works.[54,55] Specific adsorption of Cl^- ions on the TiO_2 surface could be responsible for slight changes in pH_{PZC} values.[54]

Fig. 4 shows the correlation between the rate constant for DMMP degradation and content of TiO_2 in samples (black line), whereas the blue line shows a correlation between the amount of hydroxyl groups and content of TiO_2. As can be seen, the sample denoted as Ti080Mg020 showed the highest both the rate constant and the amount of hydroxyl groups. The results clearly show that with the increasing amount of TiO_2 in composites, not only the specific surface area (see Table S2†), but also the amount of available surface –OH groups increase significantly.

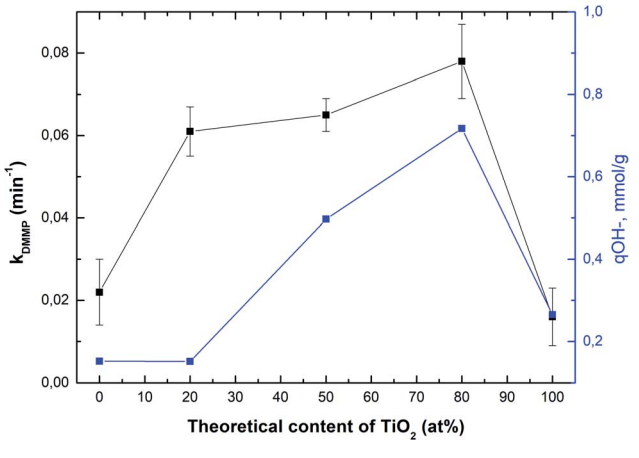

Fig. 4 Correlation between degradation rate constant of DMMP (k, min^{-1}) and the theoretical content of TiO_2, and the correlation between the amount of hydroxyl groups (q-OH, mmol g^{-1}) and the theoretical content of TiO_2.

Furthermore, TiO_2 acts also as a photocatalyst, and the highest content of hydroxyl groups could be beneficial during photocatalysis because they can serve as a source of reactive oxygen species which can attack DMMP molecule and lead to its further degradation.[56] Therefore, UV-A photocatalytic degradation of DMMP was determined on Ti100Mg000 (pure titania), Ti020Mg080, and Ti080Mg020. The results (see Fig. S11†) show that illumination slightly improves the degradation rate of all tested samples. In addition, $Mg(OH)_2$ present in the composite may acts as an electron trap and barrier for recombination, enhancing the overall photocatalytic activity of TiO_2.[57]

The acid–base properties of $TiO_2/Mg(OH)_2$ catalysts were also by adsorption of pyridine (Py) as a probe molecule. This analysis has been widely used to distinguish the presence of Lewis and/or Brønsted acid sites.[58] Fig. 5 compares the IR spectra of catalysts with different Ti and Mg ratios.

The typical vibration modes of the pyridine adsorbed species υ(CCN) appear in the frequency range between 1650 and 1400 cm^{-1}.[59] The infrared spectrum of adsorbed pyridine shows two modes which can be assigned to (i) hydrogen-bonded pyridine (hb-Py); and (ii) coordinated pyridine (L-Py).

The infrared spectrum of pure TiO_2 (Ti100Mg000) and Ti080Mg020 composite displays bands, which are indicative of the formation of L-Py species at 1604, 1574, 1492, 1444 and 1231 cm^{-1}. The coordination of Py molecules to the surface and consequent formation of L–Py indicates coordinatively unsaturated metal sites (Lewis acid sites). These bands are particularly intense in the case of pure TiO_2, that suggests strong acidity of Ti cations.

On the other hand, the formation of hydrogen-bonded Py molecules (hb-Py) suggested the bands at 1593 and 1218 cm^{-1}. As evident, these bands have low intensity on pure titania but became prominent with an increasing amount of Mg. These bands confirm the availability of H-bond donor sites (surface–OH groups with low acidity), especially on samples with higher Mg content (<50%).

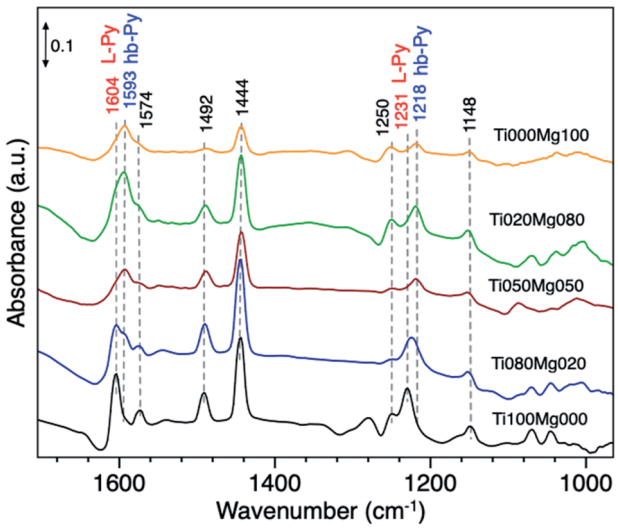

Fig. 5 FTIR spectra of adsorbed Py on TiO_2, $Mg(OH)_2$, and their composites.

In the case of DMMP degradation, DMMP molecules may react with intercalated or physisorbed water molecules which are present on the surface of catalysts (including various surface hydroxyl –OH groups), or with strong Lewis acid sites (*i.e.*, Ti^{4+}, Ti^{3+}, Mg^{2+} as was evident from XPS results) that can play an important role in the first step of DMMP adsorption.[60]

It has been reported that DMMP dissociative adsorption on MgO took place *via* nucleophilic attack,[61] where the electron-rich oxygen of P═O group of DMMP molecule interacts with coordinatively unsaturated magnesium sites (Lewis acid) or with a surface hydroxyl group. The phosphorus center of P═O bond might be subject to nucleophilic attack by the surface –OH groups. Subsequently, the loss of one methoxy group (CH_3O–) from surface-bound DMMP molecule results in formation of methanol (or formic acid) as the main volatile hydrolysis products released from the catalyst surface, and non-volatile products $[CH_3(CH_3O)P]_{ads}$ or $[CH_3(CH_3O)PO]_{ads}$ immobilized on the surface of MgO.[62]

To propose a tentative degradation mechanism for DMMP surrogate on the prepared composites, the results from *in situ* DRITS and GC-MS techniques were combined. The obtained time-resolved DRIFTS spectra for the DMMP degradation on the Ti050Mg050 sample are presented in Fig. 6. The bands were assigned according to the literature.[63,64] In the region below 1500 cm^{-1}, the presence of methoxy groups (CH_3O–) is confirmed by antisymmetric and symmetric vibrations centered at around 1460 cm^{-1}. The intensity of this band gradually decreases in time, indicating the degradation of surface adsorbed methoxy groups by their hydrolysis to gaseous methanol. Its formation indicates the absence of characteristic vibrations of the surface adsorbed metal–(OCH_3) groups in the CH region with characteristic wavenumbers at about 2850–2960 cm^{-1}. The decomposition of the methoxy groups is also manifested by the gradual extinction of $\upsilon_s(CH_3O)$ centered at 2858 cm^{-1}. At the same time, the shift of the symmetric valence vibration υ(P═O) to the lower values (1265 cm^{-1} → 1242 cm^{-1}) indicates the binding of electron-rich phosphoryl oxygen (P═O) in DMMP to the metal atom (Lewis acid) or hydroxy group (Brønsted acid).[65] The catalytic decomposition of DMMP into gaseous methanol on the surface of the composites was also confirmed by GC-MS analysis, as shown in Fig. 7.

Furthermore, the bands related to CH_3P (centered at 1315 cm^{-1}) remain very stable. This suggests the dissociation of DMMP is realized by the liberation of methoxy groups and that the final surface product (containing P-bounded methyl groups) is $[CH_3(CH_3O)P]_{ads}$.[66] Based on the DRIFTS and GC-MS analysis, the degradation mechanism was proposed in Fig. 8.

The catalytic degradation of mustard gas (HD) and its simulants (2-CEES, 2-CEPS) has been studied in detail on various metal oxides over the past 20 years.[67,68] HD detoxification include nucleophilic substitution, elimination of HCl, and oxidation through cleavage of C–Cl, and S–C bonds. The catalytic reaction of HD on the basic sites of nanostructured alumina (Al_2O_3) gives 2-chloroethyl vinyl sulfide (CEVS) and divinyl sulfide (DVS) as products.[21] Similar products were identified during degradation of 2-CEES over nanosized TiO_2,[69] MgO, and $Mg(OH)_2$.[23] DVS and 1,4-oxathiane were detected in HD reaction with AgY zeolite (the formation of 1,4-oxathiane was presumably attributed to a presence of Ag^+ ion on the surface).[70]

In our case, GC-MS analysis of the headspace extracts of the reaction mixture revealed volatile 1,2-bis(ethylthio)ethane (BETE) degradation product as suggesting *m*/*z* values 29, 35, 47, 61, 75, 89, 121 and 150 (see Fig. 9).

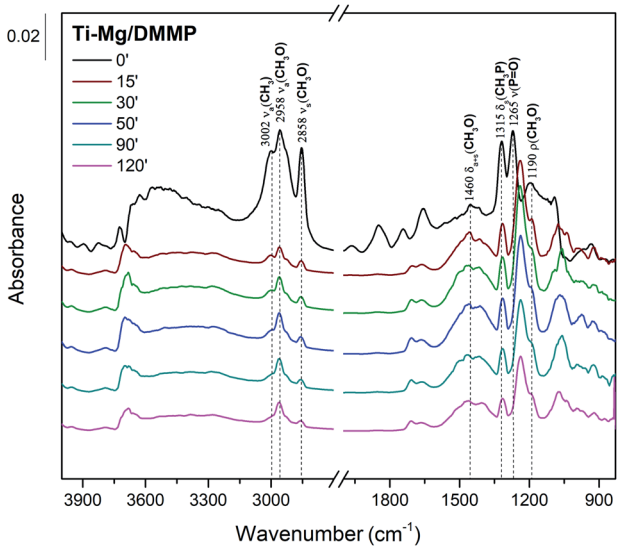

Fig. 6 Time-resolved DRIFTS spectra of DMMP adsorption on the Ti050Mg050 catalyst.

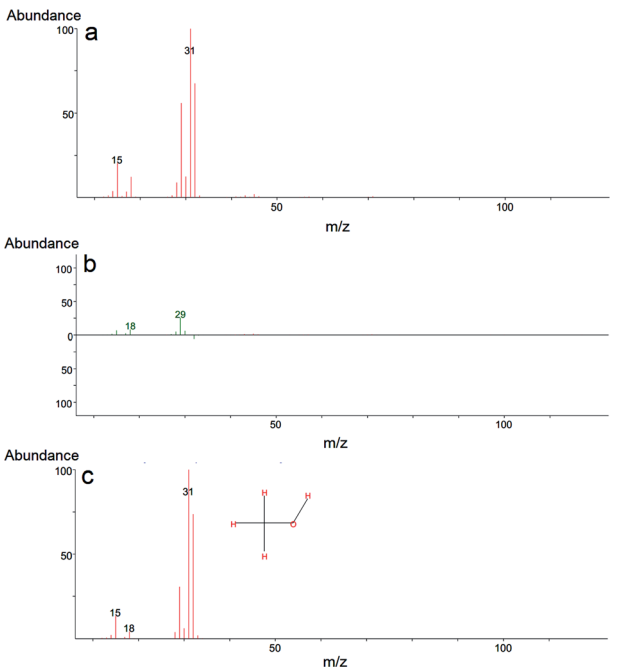

Fig. 7 Mass spectra of methanol, a degradation product of DMMP: mass spectrum obtained after degradation (a), comparison of the mass spectrum with the spectrum library (b), and the comprehensive reference mass spectrum obtained from electron-ionization (EI) library (c).

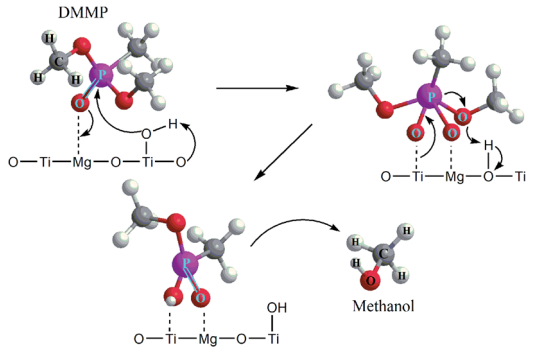

Fig. 8 The proposed mechanism of the catalytic degradation of DMMP on TiO_2/$Mg(OH)_2$ composites.

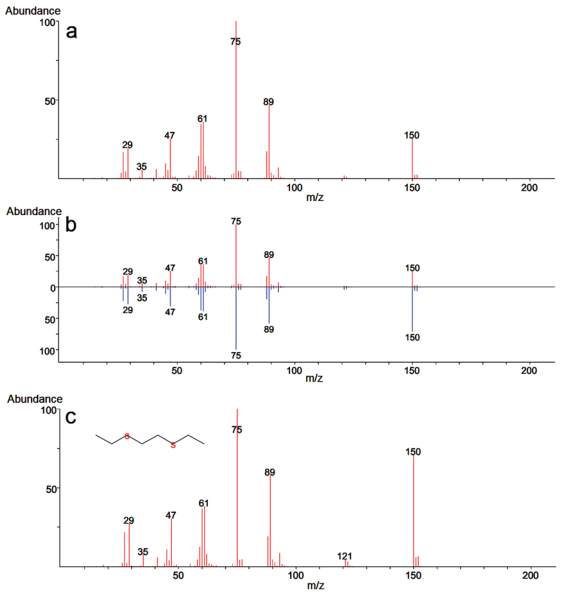

Fig. 9 Mass spectra of 1,2-bis(ethylthio)ethane (BETE), a degradation product of 2-CEES: mass spectrum obtained after degradation (a), comparison of the mass spectrum with the spectrum library (b) and the comprehensive reference mass spectrum obtained from electron-ionization (EI) library (c).

The formation of this product suggests the surface catalytic dehydrohalogenation/dimerization of 2-CEES. The reaction is initiated by the cleavage of the S–C bond and the formation of a new S–C bond between two units. Alkoxy species on the surface react with sulfonium cations (S^+), giving rise to BETE and $-OCH_2CH_3$ groups. Verma *et al.* reported the formation of EVS and alkoxy species after the interaction of 2-CEES with the hydroxyl groups on ZrO_2 (ref. 71) or WO_3 (ref. 72) nanoparticles.

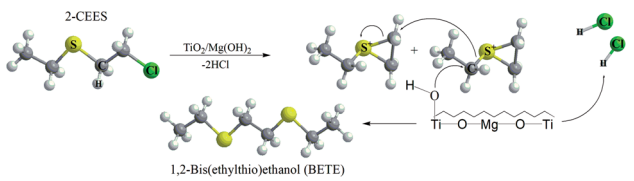

Fig. 10 The proposed mechanism of the catalytic degradation of 2-CEES on TiO_2/$Mg(OH)_2$ catalysts.

We assume that in the first step during the catalytic reaction, the intermolecular cyclization process forms a cyclic sulfonium cation (S^+). This cation is highly unstable and reacts immediately with the surface water molecules (present as surface hydroxyl groups), and by reaction with another cyclic cation forms volatile BETE. In the case of dehydrohalogenation reaction, the formation of BETE ensues from the reaction with the metal centers acting as Lewis acids and promoting the cleavage of the labile C–Cl bond in the 2-CEES molecule.[73,74] The formation of BETE was also reported in the case of interaction of 2-CEES with the Zr–OH phase[75] and zinc peroxide nanoparticles.[76] No other degradation products, such as 2-hydroxyethyl ethyl sulfide (HEES), ethyl vinyl sulfide (EVS), diethyl disulfide (DEDS), were observed in the headspace extract. The proposed degradation mechanism of 2-CEES on TiO_2/$Mg(OH)_2$ composites is shown in Fig. 10.

In the case of 2-CEPS degradation, GC-MS analysis show fragmentation pattern with *m*/*z* 18, 27, 39, 45, 51, 58, 65, 77, 84, 91, 103, 109, 121 and 135 assigned to phenyl vinyl sulfide (PVS) as the primary degradation product (see Fig. 11). Similarly to 2-CEES degradation, the cyclic sulfonium cation is also the promoter of the reaction. Prasad *et al.* (2010) studied in detail the degradation of 2-CEPS with metal-based nano-oxides AP–Al_2O_3, AP–Al_2O_3–Fe_2O_3, or AP–Al_2O_3–V_2O_5 by using GC-MS and infrared spectroscopy. In this case, the 2-CEPS molecule reacts with Al_2O_3 and Al_2O_3–Fe_2O_3 in two ways: (i) with surface hydroxyl groups (or physisorbed water molecules) to 2-ethyl phenyl sulfide (2-HEPS); (ii) formation of surface-bound alkoxides. On the contrary, on Al_2O_3–V_2O_5, 2-CEPS can react: (i) with hydroxyl groups to 2-HEPS; (ii) with V^{+5} acidic sites forming sulphoxide of 2-CEPS and (iii), with V–OH giving surface alkoxy

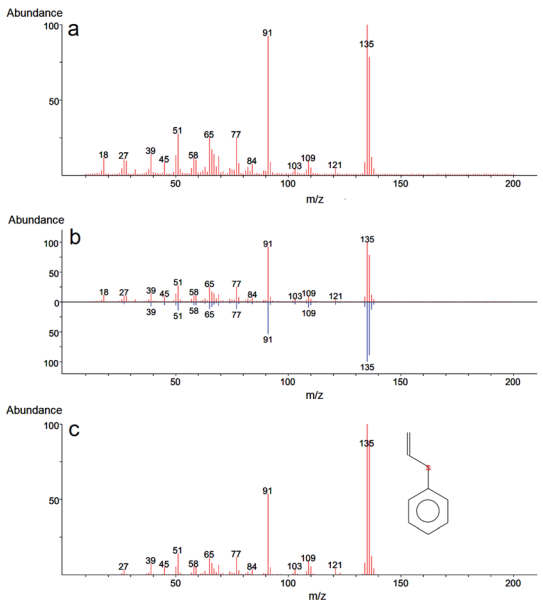

Fig. 11 Mass spectra of phenyl vinyl sulfide (PVS), a degradation product of 2-CEPS: mass spectrum obtained after degradation (a), comparison of the mass spectrum with the spectrum library (b), and comprehensive reference mass spectrum obtained from electron-ionization (EI) library (c).

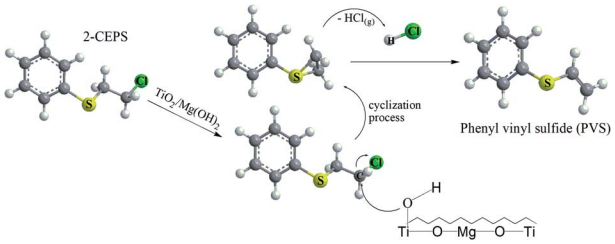

Fig. 12 The proposed mechanism of the catalytic degradation of 2-CEPS on $TiO_2/Mg(OH)_2$ catalysts.

species.[77] Based on the literature and our GC-MS investigation, the possible mechanism of the 2-CEPS interaction with the $TiO_2/Mg(OH)_2$ surface was proposed (see Fig. 12). 2-CEPS molecule adsorbs on the Brønsted acid sites. In this step, hydrogen from the surface hydroxyl group attacks the sulphur or chlorine atom of the 2-CEPS molecule and promotes the intermolecular cyclization process forming cyclic sulfonium cation (S^+).

Then, the dehydrohalogenation reaction occurs, and the chlorine atom is eliminated (as HCl). At the same time, the lattice oxygen atom (the electron-rich oxygen O^{2-}) attacks the acidic hydrogen affiliated to the carbon atom (neighbour of the sulphur atom in CEPS molecule). Subsequent elimination leads to the formation of degradation product (PVS) *via* surface bonded alkoxy species.[78] The PVS has lower toxicity in comparison with 2-CEPS.[79] Similar results were reported in several other studies.[80,81] In our case, no other degradation products, such as hydroxyl ethyl phenyl sulphide (HEPS), have been identified in the headspace extract.

Conclusions

In this work, we have introduced $TiO_2/Mg(OH)_2$ composites that were used for the rapid degradation of CWA surrogates DMMP, 2-CEES, and 2-CEPS in aqueous solution. Mixing TiO_2 and $Mg(OH)_2$ has been found to rapidly increase the specific surface area and degradation activity of the resulting composites. One of the most important catalyst parameters – acid–base properties were correlated with the activity of the samples. The acidity and amount of –OH groups, as well as the specific surface area are decisive factors for the degradation of DMMPs and were strongly affected by Ti : Mg ratio.

Moreover, titanium dioxide in the composites can further promote degradation of CWA surrogates by photocatalysis. Based on the analysis of the degradation products, the mechanism for degradation of the used surrogates was proposed and discussed with the available literature. From these results, we infer that mixed-metal oxides and composites represent a promising way how to rapidly and safely decompose highly toxic compounds by surface chemical reactions.

Conflicts of interest

There are no conflicts to declare.

Acknowledgements

Czech Academy of Sciences-Bulgarian Academy of Sciences bilateral project (BAS-20-11) and financial support of Project No. DFNP-17-61/26.07.2017 are acknowledged. The authors acknowledge the assistance provided by the Research Infrastructure NanoEnviCz, supported by the Ministry of Education, Youth and Sports of the Czech Republic under Project No. LM2018124. Authors thank to Dr Darina Smržová and Michaela Šrámová-Slušná for nitrogen physisorption measurements.

References

1 K. Kuča, M. Pohanka, in *Molecular, Clinical and Environmental Toxicology: Volume 2: Clinical Toxicology*, ed. A. Luch, Birkhäuser Basel, Basel, 2010, pp. 543–558.
2 K. Ganesan, S. K. Raza and R. Vijayaraghavan, *J. Pharm. BioAllied Sci.*, 2010, **2**, 166–178.
3 G. W. Wagner, *Ind. Eng. Chem. Res.*, 2011, **50**, 12285–12287.
4 B. C. Singer, A. T. Hodgson, H. Destaillats, T. Hotchi, K. L. Revzan and R. G. Sextro, *Environ. Sci. Technol.*, 2005, **39**, 3203–3214.
5 A. K. Verma, A. K. Srivastava, B. Singh, D. Shah, S. Shrivastava and C. K. P. Shinde, *Chemosphere*, 2013, **90**, 2254–2260.
6 T. H. Mahato, G. K. Prasad, B. Singh, K. Batra and K. Ganesan, *Microporous Mesoporous Mater.*, 2010, **132**, 15–21.
7 V. Štengl, M. Maříková, S. Bakardjieva, J. Šubrt, F. Opluštil and M. Olšanská, *J. Chem. Technol. Biotechnol.*, 2005, **80**, 754–758.
8 V. Štengl, J. Bludská, F. Opluštil and T. Němec, *Mater. Res. Bull.*, 2011, **46**, 2050–2056.
9 V. Šteng, M. Maříková, S. Bakardjieva, J. Šubrt, F. Opluštil and M. Olšanská, *J. Chem. Technol. Biotechnol.*, 2005, **80**, 754–758.
10 G. W. Wagner, O. B. Koper, E. Lucas, S. Decker and K. J. Klabunde, *J. Phys. Chem. B*, 2000, **104**, 5118–5123.
11 B. Nazari and M. Jaafari, *Dig. J. Nanomater. Bios.*, 2010, **5**, 909–917.
12 V. Štengl, V. Houšková, S. Bakardjieva, N. Murafa, M. Maříková, F. Opluštil and T. Němec, *Mater. Charact.*, 2010, **61**, 1080–1088.
13 M. Šťastný, V. Štengl, J. Henych, J. Tolasz, P. Vomáčka and J. Ederer, *J. Mater. Sci.*, 2016, **51**, 2634–2642.
14 P. Janoš, T. Hladík, M. Kormunda, J. Ederer and M. Šťastný, *Adv. Mater. Sci. Eng.*, 2014, **2014**, 1–24.
15 P. Janos, P. Kuran, M. Kormunda, V. Stengl, T. M. Grygar, M. Dosek, M. Stastny, J. Ederer, V. Pilarova and L. Vrtoch, *J. Rare Earths*, 2014, **32**, 360–370.
16 N. Sharma and R. Kakkar, *J. Comput. Sci.*, 2015, **10**, 225–236.
17 G. W. Wagner, P. W. Bartram, O. Koper and K. J. Klabunde, *J. Phys. Chem. B*.
18 L. Bigiani, D. Zappa, D. Barreca, A. Gasparotto, C. Sada, G. Tabacchi, E. Fois, E. Comini and C. MacCato, *ACS Appl. Mater. Interfaces*, 2019, **11**(26), 23692–23700.
19 J. R. Soliz, W. O. Gordon, A. Balboa, J. Mahle, A. J. Hauser, K. M. Bussmann, M. S. Osofsky and C. J. Karwacki, in

Abstracts of Papers, 250th ACS National Meeting & Exposition, Boston, MA, United States, August 16-20, 2015.
20 G. K. Prasad, P. V. R. K. Ramacharyulu, J. Praveen Kumar, K. Ganesan and B. Singh, *J. Sci. Ind. Res.*, 2012, **71**, 205–209.
21 N. Sharma and R. Kakkar, *Adv. Mater.*, 2013, **4**, 508–521.
22 K. J. Ewing and B. Lerner, *Appl. Spectrosc.*, 2001, **55**, 407–411.
23 B. Maddah and H. Chalabi, *Int. J. Nanosci. Nanotechnol.*, 2012, **8**, 157–164.
24 R. M. Narske, K. J. Klabunde and S. S. Fultz, *Abstr. Pap. 221st ACS Natl. Meet*, San Diego, CA, United States, April 1-5, 2001, IEC-318.
25 V. Štengl, S. Bakardjieva, M. Maříková, P. Bezdička and J. Šubrt, *Mater. Lett.*, 2003, **57**, 3998–4003.
26 V. Štengl, T. M. Grygar, F. Opluštil and T. Němec, *J. Hazard. Mater.*, 2011, **192**, 1491–1504.
27 J. Henych, P. Janoš, M. Kormunda, J. Tolasz and V. Štengl, *Arabian J. Chem.*, 2016, **11**, 4258–4269.
28 G. D. Bukatov, D. K. Maslov, S. A. Sergeev and M. A. Matsko, *Appl. Catal., A*, 2019, **577**, 69–75.
29 Y. Liu, J. Zou, X. Zeng and W. Ding, *RSC Adv.*, 2014, **4**, 42764–42771.
30 H. Jeon, Y. J. Min, S. H. Ahn, S.-M. Hong, J.-S. Shin, J. H. Kim and K. B. Lee, *Colloids Surf., A*, 2012, **414**, 75–81.
31 C. H. Ashok, V. K. Rao and C. H. Shilpa Chakra, *J. Nanomed. Nanotechnol.*, 2015, **06**, 2–6.
32 P.-Y. Wu, Y.-P. Jiang, Q.-Y. Zhang, Y. Jia, D.-Y. Peng and W. Xu, *New J. Chem.*, 2016, **40**, 2878–2885.
33 M. Hua, S. Zhang, B. Pan, W. Zhang, L. Lv and Q. Zhang, *J. Hazard. Mater.*, 2012, **211–212**, 317–331.
34 A. Dhanya and K. Aparna, in *Recent Advances in Chemical Engineering: Select Proceedings of ICACE 2015*, ed. I. Regupathi, V. K. Shetty and M. Thanabalan, Springer Singapore, Singapore, 2016, pp. 219–225.
35 J. Bandara, S. S. Kuruppu and U. W. Pradeep, *Colloids Surf., A*, 2006, **276**, 197–202.
36 H. S. Jung, J.-K. Lee, M. Nastasi, S.-W. Lee, J.-Y. Kim, J.-S. Park, K. S. Hong and H. Shin, *Langmuir*, 2005, **21**, 10332–10335.
37 C. S. Chou, R. Y. Yang, C. K. Yeh and Y. J. Lin, *Powder Technol.*, 2009, **194**, 95–105.
38 a. L. Patterson, *Phys. Rev.*, 1939, **56**, 978–982.
39 M. Naderi, in *Progress in Filtration and Separation*, 2014, pp. 585–608.
40 J. Henych, P. Janoš, M. Kormunda, J. Tolasz and V. Štengl, *Arabian J. Chem.*, 2016, **11**, 4258–4269.
41 M. Šťastný, J. Tolasz, V. Štengl, J. Henych and D. Žižka, *Appl. Surf. Sci.*, 2017, **412**, 19–28.
42 S. Ardizzone, C. L. Bianchi, M. Fadoni and B. Vercelli, *Appl. Surf. Sci.*, 1997, **119**, 253–259.
43 D. E. Haycock, M. Kasrai, C. J. Nicholls and D. S. Urch, *J. Chem. Soc., Dalton Trans.*, 1978, 1791–1796.
44 M. Giannini, T. B. Ballaran and F. Langenhorst, *Am. Mineral.*, 2014, **99**, 2060–2067.
45 S. Feliu Jr, J. C. Galván, A. Pardo, M. C. Merino and R. Arrabal, *Open Corros. J.*, 2010, **3**, 80–91.
46 J. Henych, V. Stengl, A. Mattsson and L. Osterlund, *Photochem. Photobiol.*, 2015, **91**, 48–58.
47 M. Šťastný, J. Tolasz, V. Štengl, J. Henych and D. Žižka, *Appl. Surf. Sci.*, 2017, **412**, 19–28.
48 L. Forni, *Catal. Rev.*, 1974, **8**, 65–115.
49 T. Preočanin and N. Kallay, *Croat. Chem. Acta*.
50 C. Contescu, J. Jagiełło and J. A. Schwarz, *Langmuir*, 1993, **9**, 1754–1765.
51 M. N. Khan and A. Sarwar, *Surf. Rev. Lett.*, 2007, **14**, 461–469.
52 S. Yang, D. Shao, X. Wang and M. Nagatsu, *RSC Adv.*, 2014, **4**, 4856–4863.
53 H. Kawakami and S. Yoshida, *J. Chem. Soc., Faraday Trans. 2*, 1984, **80**, 921–932.
54 J. P. Reymond and F. Kolenda, in *Powder Technology*, 1999.
55 K. Bourikas, C. Kordulis and A. Lycourghiotis, *Environ. Sci. Technol.*, 2005, **39**, 4100–4108.
56 K. E. O'Shea, I. Garcia and M. Aguilar, *Res. Chem. Intermed.*, 1997, **23**, 325–339.
57 J. Bandara, C. C. Hadapangoda and W. G. Jayasekera, *Appl. Catal., B*, 2004, **50**, 83–88.
58 A. Penkova, L. F. Bobadilla, F. Romero-Sarria, M. A. Centeno and J. A. Odriozola, *Appl. Surf. Sci.*, 2014, **317**, 241–251.
59 E. Selli and L. Forni, *Microporous Mesoporous Mater.*, 1999, **31**, 129–140.
60 C. N. Rusu and J. T. Yates, *J. Phys. Chem. B*, 2000, **104**, 12292–12298.
61 G. E. Fryxell and G. Cao, *Environmental applications of nanomaterials: Synthesis, sorbents and sensors*, 2nd edn, 2012.
62 M. B. Mitchell, V. N. Sheinker, W. W. Cox, E. N. Gatimu and A. B. Tesfamichael, *J. Phys. Chem. B*, 2004, **108**, 1634–1645.
63 K. Knagge, M. Johnson, V. H. Grassian and S. C. Larsen, *Langmuir*, 2006, **22**, 11077–11084.
64 S. R. Segal, L. Cao, S. L. Suib, X. Tang and S. Satyapal, *J. Catal.*, 2001, **198**, 66–76.
65 A. R. Head, R. Tsyshevsky, L. Trotochaud, Y. Yu, L. Kyhl, O. Karslloğlu, M. M. Kuklja and H. Bluhm, *J. Phys. Chem. C*, 2016, **120**, 29077–29088.
66 W. C. Hung, J. C. Wang and K. H. Wu, *Appl. Surf. Sci.*, 2018, **444**, 330–335.
67 M. E. Martin, R. M. Narske and K. J. Klabunde, *Microporous Mesoporous Mater.*, 2005, **83**, 47–50.
68 S. C. Stout, S. C. Larsen and V. H. Grassian, *Microporous Mesoporous Mater.*, 2007, **100**, 77–86.
69 I. N. Martyanov and K. J. Klabunde, *Environ. Sci. Technol.*, 2003, **37**, 3448–3453.
70 G. W. Wagner and P. W. Bartram, *Langmuir*, 1999, **15**, 8113–8118.
71 M. Verma, R. Chandra and V. K. Gupta, *J. Environ. Chem. Eng.*, 2016, **4**, 219–229.
72 M. Verma, R. Chandra and V. K. Gupta, *J. Colloid Interface Sci.*, 2015, **453**, 60–68.
73 S.-T. Han, H.-L. Xi, X.-Z. Fu, X.-X. Wang, Z.-X. Ding, Z.-C. Lin and W.-Y. Su, *Wuli Huaxue Xuebao*, 2004, **20**, 296–301.
74 B. W. L. Jang and J. J. Spivey, *Catal. Today*, 2000, **55**, 3–10.
75 J. K. Mitchell, J. A. Arcibar-Orozco and T. J. Bandosz, *Appl. Surf. Sci.*, 2016, **390**, 735–743.
76 D. A. Giannakoudakis, M. Florent, R. Wallace, J. Secor, C. Karwacki and T. J. Bandosz, *Appl. Catal., B*, 2018, **226**, 429–440.

77 G. K. Prasad, *J. Sci. Ind. Res.*, 2010, **69**, 835–840.
78 G. W. Wagner and Y.-C. Yang, *Ind. Eng. Chem. Res.*, 2002, **41**, 1925–1928.
79 M. J. Climent, A. Corma, S. Iborra and A. Velty, *J. Mol. Catal. A: Chem.*, 2002, **182–183**, 327–342.
80 M. Sadeghi, S. Yekta and H. Ghaedi, *Int. Nano Lett.*, 2016, **6**, 161–171.
81 A. Kiani and K. Dastafkan, *J. Colloid Interface Sci.*, 2016, **478**, 271–279.